Metal-to-Multilayer-Graphene Contact—Part I: Contact Resistance Modeling

Yasin Khatami, *Student Member, IEEE*, Hong Li, *Student Member, IEEE*, Chuan Xu, *Member, IEEE*, and Kaustav Banerjee, *Fellow, IEEE*

***Abstract*—Parasitic components are becoming increasingly important with geometric scaling in nanoscale electronic devices and interconnects. The parasitic contact resistance between metal electrodes and multilayer graphene (MLG) is a key factor determining the performance of MLG-based structures in various applications. The available methods for characterizing metal–MLG contact interfaces rely on a model based on the top-contact structure, but it ignores the edge contacts that can greatly reduce the contact resistance. Therefore, in the present work, a rigorous theoretical 1-D model for metal–MLG contact is developed for the first time. The contribution of the major components of resistance—the top and edge contacts (side and end contacts) and the MLG sheet resistivity—to the total resistance of the structure is included in the model. The 1-D model is compared to a 3-D model of the system, and a method for investigation and optimization of the range of validity of the 1-D model is developed. The results of this work provide valuable insight to both the characterization and design of metal–MLG contacts.**

***Index Terms*—Contact resistance, edge contact, multilayer graphene (MLG), top contact, 1-D contact model.**

I. Introduction

GRAPHENE, which is a single atomic layer of sp^2 hybridized carbon atoms arranged in a honeycomb structure, has become one of the most researched materials in the electronics community in recent years due to its superb electrical and thermal properties. Graphene has ultrahigh mobility (200 000 $\text{cm}^2/\text{V} \cdot \text{s}$ theoretically) and excellent electrostatic controllability by a gate electrode [1]–[6]. Single-layer graphene (SLG) has a breaking strength 200 times greater than that of steel and a relatively high tensile strength [7], as well as high thermodynamic stability [1]–[6]. Due to its remarkable properties, the International Technology Working Group (ITRS) has selected carbon-based nanoelectronics, including graphene, as promising technologies in the emerging devices and materials category [8]. Graphene exhibits very high current density due to its sp^2 hybridized bonds and higher reliability due to better electromigration tolerance compared to copper [9]–[17]. It is also demonstrated that graphene's current-carrying capacity can be further enhanced by sp^2-on-sp^3 technology [18]. Compared to copper, graphene has higher thermal conductivity [19], [20] and a large carrier mean free path, which leads to higher conductance [10], [11], [19]. Multilayer graphene (MLG) has gained a lot of attention in recent years in device and interconnect applications. MLG exhibits transport properties superior to those of SLG due to its higher number of conducting channels and higher band overlap [9]–[13]. Furthermore, the substrate has a much smaller impact on the graphene layers for MLG compared to SLG. In addition, the bandgap opening in bi- and trilayer graphene has attracted researchers into the use of MLG in device and memory applications [21]–[26]. Graphene is a highly flexible material with high transparency, which makes it an excellent alternative to indium tin oxide as a transparent electrode for light-emitting diodes, solar cells, touchpad displays, and memory devices [27]–[35]. Graphene can also be used in communications applications in amplifier and phase detector blocks [36], [37]. It has been shown that the metal–graphene contact contributes to noise in graphene transistors, and MLG is known to exhibit lower $1/f$ noise compared to SLG [38], [39]. In [39], a new type of graphene device is proposed and demonstrated that incorporates the low-noise metal–MLG contact with an SLG channel. The so-called graphene thickness-graded transistor combines the benefit of high mobility in SLG with low contact noise of MLG.

While graphene exhibits excellent electrical and thermal properties, graphene-based structures exhibit poor electrical transport properties due to the impacts of parasitic components. Contact resistance is one of the most important parasitic components in graphene-based electronic structures, including devices and interconnects. Therefore, it is important to understand the dependence of contact resistance on different device parameters. Although many researchers have focused on metal–SLG contact [40]–[66], little is known about the properties of metal–MLG contacts. The metal-to-SLG/MLG contact characterization is reported in [45]–[52], [67], and [68]. The type of analysis used to extract the individual resistivity values is usually based on a method called transmission line method (TLM) similar to that in [69] and [70], where the top-contact type is assumed for a metal–MLG structure. Although this method can be used for metal–SLG structures with relatively accurate results, it will be shown here and in the companion

Manuscript received March 21, 2012; revised May 25, 2012; accepted June 8, 2012. Date of current version August 17, 2012. This work was supported by the National Science Foundation under Grant CCF-0811880. The review of this paper was arranged by Editor D. Esseni.

Y. Khatami, H. Li, and K. Banerjee are with the Department xof Electrical and Computer Engineering, University of California at Santa Barbara, Santa Barbara, CA 93106 USA (e-mail: yasin@ece.ucsb.edu; hongli@ece.ucsb.edu; kaustav@ece.ucsb.edu).

C. Xu was with the Department of Electrical and Computer Engineering, University of California at Santa Barbara, Santa Barbara, CA 93106 USA. He is now with the Technology Development and Innovation Group, Maxim Integrated Products, Beaverton, OR 97005 USA (e-mail: Chuan.Xu@maxim-ic.com).

Color versions of one or more of the figures in this paper are available online at http://ieeexplore.ieee.org.

Digital Object Identifier 10.1109/TED.2012.2205256

0018-9383/$31.00 © 2012 IEEE

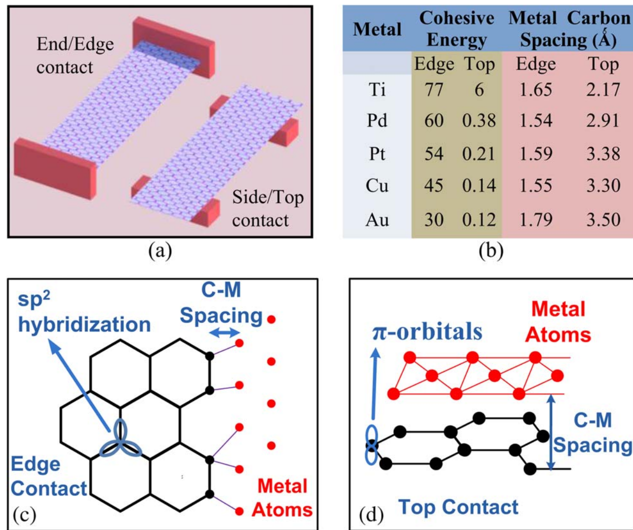

Metal	Cohesive Energy		Metal Carbon Spacing (Å)	
	Edge	Top	Edge	Top
Ti	77	6	1.65	2.17
Pd	60	0.38	1.54	2.91
Pt	54	0.21	1.59	3.38
Cu	45	0.14	1.55	3.30
Au	30	0.12	1.79	3.50

Fig. 1. Metal–graphene contact. (a) Schematic illustration of side (top)- and end (edge)-contacted metal–graphene structures. (b) Cohesive energy and metal–carbon spacing in edge- and top-contact structures [59] for different metals. Cohesive energy is given in kilocalories per mole. Schematic illustrations of (c) edge- and (d) top-contact structures. The sp^2 hybridization of graphene is illustrated in (c). The C–M spacing in (c) and (d) represents the distance between metal and carbon atoms.

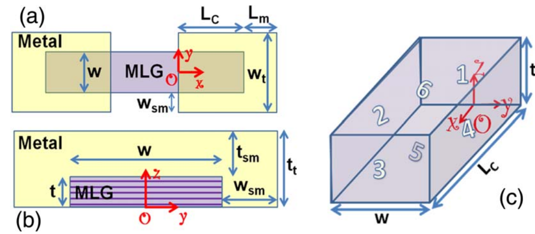

Fig. 2. Schematic views of metal contact to MLG. (a) View from top (x–y plane). (b) Cross-sectional view (y–z plane). (c) Labeling of the MLG sides. Metal covers the sides 2, 3, 4, and 6. The sides 2 to 6 represent the outer surface of the MLG sheet under the contact. Side 1 is at $x = 0$, at the beginning of the channel, and the symbol "O" shows the origin.

paper (part II) [71] that it cannot model the metal–MLG contact accurately due to the presence of *edge contacts*.

In a metal–MLG structure, the metal–graphene contact for the topmost graphene sheet is of both side/top- and end/edge-contact types [Fig. 1(a)], while metal only contacts the underlying graphene layers through an end/edge contact. The schematic illustration of the side and end contacts is shown in Fig. 1(a). Fig. 2(a) and (b) further show the contact between the metal and graphene layers. To simplify the terminology, the terms "top contact" and "edge contact" will be used here to refer to the side and end contacts, respectively. It has been shown that the edge contact for metal–carbon-nanotube structures substantially reduces the contact resistance compared to side contacts [72]–[75]. Similarly, the first-principle calculations show that the edge-contacted metal–SLG structure exhibits a contact resistance substantially smaller than that of the top-contacted metal–SLG structures [59], [60]. The improvement in contact resistivity, reported as the ratio of the contact resistance per carbon atom for top contact to that for edge contact, varies between 10 and 10 000, depending on the type of metal [59]. This improvement is attributed to the smaller gap formed between metal and carbon atoms in edge-contacted structures and the contribution of $p\pi$ and $p\sigma$ orbitals to conduction.

The schematic illustrations of the edge and top contacts are shown in Fig. 1(c) and (d), respectively, where the C–M spacing shows the gap between carbon and metal atoms. Carbon atoms form sp^2 bonding in graphene. Therefore, each carbon atom shares three electrons with the nearest neighboring carbon atoms in the basal plane in the form of three sigma bonds. The other electron in the $2p$ atomic orbital overlaps with those of its nearest neighbors to form a π bonding system. The π orbitals are perpendicular to the basal plane as shown in Fig. 1(d). However, the carbon atoms at the edges of graphene can form only two sigma bonds with the neighboring carbon atoms. Therefore, the metal atoms connected to the edges of graphene [Fig. 1(c)] can form a stronger bond to carbon atoms compared to the metal atoms in the top-contact structure [Fig. 1(d)]. This phenomenon can be studied through the calculation of the cohesive energy of the system [59], [60]. The cohesive energy of the interface between metal and carbon atoms and the metal–carbon spacing are listed in Fig. 1(b) for different types of metals. It can be observed that the edge-contact interface provides higher cohesive energy compared to the side-contact interface. Higher cohesive energy leads to a smaller spacing between metal and carbon atoms. The carrier transport across the metal–graphene interface can be treated as a quantum tunneling process. In a tunneling process, the smaller the width of the tunneling barrier, the higher the tunneling probability [76]. Henceforth, the edge-contact structure exhibits smaller contact resistivity. As the number of graphene layers increases in a metal–MLG structure, the contribution of edge contacts to electrical conduction increases dramatically. In the companion paper [71], it will be shown that the regular characterization analysis based on the top-contact model [45]–[52], [67], [68] does not model the metal–MLG structures accurately.

Furthermore, in MLG, the nature of electrical transport in the basal plane is different from that along the c-axis, where the c-axis is the direction perpendicular to the basal plane (graphene layers). In the basal plane, the π-orbital electrons are responsible for conductance, while the thermal excitation of carriers along the layers and impurity-assisted interlayer hopping are the primary sources for the c-axis conduction [77]. Therefore, MLG exhibits anisotropic conductance along the basal plane and the c-axis [78]. Due to this anisotropy and the presence of edge contacts, the metal–MLG structure is a full 3-D system. Hence, a new model needs to be developed that can capture the effects of different parameters on the resistance of the 3-D metal–MLG structure.

In this work, a new model is developed, which is based on a comprehensive analysis of the effects of both the top and edge contacts on the overall performance of the metal–MLG structure. The role of different parameters such as the geometry of the structure and the sheet resistivity on the total resistance of the system is presented. A simplified 1-D model is developed that captures the effects of the edge and top contacts and the sheet resistivity of graphene and matches well with the 3-D model. The 1-D model is shown to be useful in understanding the contribution of different parameters to the total resistance and the current flow path in the system. The total resistance

of the metal–MLG structures is studied by assuming diffusive transport. This assumption is valid when graphene dimensions are much larger than the carrier mean free path. The implication of the developed model for the quasi-ballistic regime is discussed in the companion paper [71].

The developed model is based on distributed contact. The validity of the distributed contact is discussed in [81]. Recent experimental results on the contact resistance of metal–SLG structures [82] further support the validity of the distributed model.

First, the metal–MLG contact structure and the modeling assumptions are presented in Section II. Then, in Section III, the structure is studied under the assumption that the metal resistance is negligible. This assumption is helpful in understanding the role of edge contacts on the overall characteristics of the contact and in developing the 1-D model. The 3-D model and the 1-D model are developed in Section III, and the comparison of the two models and the range of validity of the 1-D model are investigated.

Then, in the companion paper [71], the 1-D model is expanded to include the effect of metal resistivity. The 1-D model is applied to different metal–MLG structures. The three major components of the total resistance—metal sheet resistance, MLG sheet resistance, and contact resistance—are studied together, and the importance of these resistances for different geometries is studied. The developed model is further described in the quasi-ballistic regime. This type of analysis is invaluable for both the characterization and design of MLG-based structures that involve top and edge contacts.

II. Metal–MLG Contact Structure

The metal–MLG structure is shown in Fig. 2(a) and (b). Two metal electrodes are connected to an MLG structure. Fig. 2(a) shows the top view, and Fig. 2(b) shows a cross section of the contact in the y–z plane. In Fig. 2, w and t are the width and thickness of the MLG sheet, respectively, L_C is the contact length, w_{sm} and t_{sm} are the width and thickness of the side metal, respectively, and L_m is the length of the extension of the metal. In Fig. 2(c), the MLG sheet under the metal electrode is shown as a box. The labeling of the sides will be used later on as a convenience to define the boundary conditions (BCs). The metal covers the sides 2, 3, 4, and 6, and side 1 is at the beginning of the channel region. The contact to the graphene layers is of the edge-contact type, while the topmost layer has both the top and edge contacts.

The graphene width is large enough (> 200 nm) so that edge scattering and quantum mechanical effects resulting from width confinement can be ignored. The properties of graphene can be affected by substrate, contact, and charge impurities. The substrate becomes important, particularly when the number of layers is small. It has been shown that the charge screening length in MLG is between 0.5 and 1 nm [14], [79], [83]. Therefore, the substrate effect only becomes important for an MLG thickness of less than 1 nm. Suspending graphene [3], [4], [52] or vacuum annealing of graphene [45]–[52] has been shown to reduce the substrate effects significantly. The substrate effects are not included in this paper, and depending on the structure and the method used for fabrication of the MLG structure, one might need to implement the substrate effects into the model (i.e., through modification of the MLG sheet resistivity).

Furthermore, it has been shown that the metal contacts can alter the Fermi level and the density of states of graphene [40]–[44], [53], [54], [84], which leads to a change in the sheet resistivity of graphene under metal. Therefore, the contact resistance, which is determined by the slope of the I–V curve near the Fermi level, becomes strongly dependent on the type of metal. In this work, the MLG under the contact is studied; thus, an effective sheet resistivity in conjunction with an effective contact resistivity is considered for MLG under the contact. To understand the overall effects of these nonidealities, in this work, a wide range of MLG sheet resistivity and contact resistivity is studied. Moreover, it is assumed that the total voltage applied to the structure is less than 0.1 V; hence, the Fermi-level variation inside graphene is small. Due to the exclusion of the channel in the developed 1-D model, the asymmetry of conduction in the hole- and electron-dominated transport regimes in graphene-based field-effect transistors [17], [53], [54] is not modeled in this work.

III. Model for Negligible Metal Resistance

In this section, the metal resistance is assumed to be negligible compared to the sheet resistance of MLG. Considering the typical values of metal resistivity (ρ_m) for copper and gold of around $2 \times 10^{-8}\ \Omega \cdot \mathrm{m}$ [80] and a basal plane sheet resistivity of graphene (ρ_s) of around $5 \times 10^{-7}\ \Omega \cdot \mathrm{m}$ [78], the assumption of negligible metal resistance is valid, when the area of metal is much larger than that of MLG. In this section, ρ_s is assumed to be larger than $5 \times 10^{-7}\ \Omega \cdot \mathrm{m}$, because lower values of ρ_s lead to inaccurate results when ρ_m is ignored. The lower values of ρ_s are considered in the companion paper [71], where the model including the metal resistivity is developed. The ratio of top-contact resistivity per carbon atom to edge-contact resistivity per carbon atom is assumed to vary between 0.01 and 10 000 and is represented by the parameter f.

A. Model Derivation

1) Three-Dimensional Model: To model the contact resistance to an MLG sheet, a simple device structure consisting of two metal contacts deposited on two ends of an MLG sheet is used [Fig. 2(a)]. The use of the following model requires the assumption that the contacts are ohmic. The MLG body and the metal–MLG interfaces are modeled by resistive elements. The MLG sheet is modeled by an infinite number of basic resistive elements, where six resistors are connected to each node as shown in Fig. 3, and the contact resistances are modeled by resistive elements between metal and MLG nodes. The resistivity ρ_s is the basal plane electrical resistivity of MLG in $\Omega \cdot \mathrm{m}$, and ρ_I is the c-axis electrical resistivity of MLG in $\Omega \cdot \mathrm{m}$. The ratios ρ_I/ρ_s are 100 to 170 for natural single-crystal graphite, 2500 to 8800 for pyrolytic graphite, and 180 to 210 for kish graphite [78]. In this paper, a value of $\rho_I/\rho_s = 100$ is chosen.

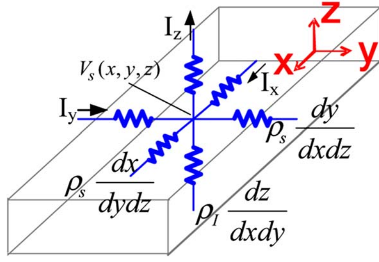

Fig. 3. Resistive network model for the MLG sheet. The aforementioned model is used for each node in the MLG sheet after discretization of the MLG sheet.

The following equations define the currents in each resistive element according to Ohm's law ($I = V/R$):

$$I_x = \frac{-dydz}{\rho_s}\frac{dV_S}{dx} \tag{1}$$

$$I_y = \frac{-dxdz}{\rho_s}\frac{dV_S}{dy} \tag{2}$$

$$I_z = \frac{-dxdy}{\rho_I}\frac{dV_S}{dz}. \tag{3}$$

The potential at each node is $V_S(x, y, z)$, and I_x, I_y, and I_z represent the electrical currents in the x-, y-, and z-directions, respectively. At each node

$$dI_x + dI_y + dI_z = 0. \tag{4}$$

By combining (1)–(4), the partial differential equation (PDE) for the system is

$$\frac{1}{\rho_s}\frac{d^2V_S}{dx^2} + \frac{1}{\rho_s}\frac{d^2V_S}{dy^2} + \frac{1}{\rho_I}\frac{d^2V_S}{dz^2} = 0. \tag{5}$$

The solution to (5) gives the potential (V_S) in the MLG body. Next, the BCs need to be introduced. The coordinate axis is shown in Fig. 2, and the origin is marked with the symbol O. Due to the symmetry of the device along the y-axis, only half of the structure from $y = 0$ to $y = w/2$ is studied. Because of the symmetry, I_y is zero at $y = 0$. At side 4 ($y = w/2$), I_y is calculated as the voltage drop on the contact resistance divided by the value of the contact resistance. The contact at this edge is of the edge-contact type, and its value is $\rho_e/dxdz$, where ρ_e is the edge-contact resistivity in $\Omega \cdot \mathrm{m}^2$.

The contact resistivity per carbon atom for top and edge contacts (ρ_{c_pc} and ρ_{e_pc}, respectively) is reported in [59] for different metals by the use of first-principle calculations, where ρ_{e_pc} is found to be much smaller than ρ_{c_pc}. Here, the parameter f is defined as $f = \rho_{c_\mathrm{pc}}/\rho_{e_\mathrm{pc}}$, which is a dimensionless parameter. The dependence of f on the metal–carbon spacing can be understood from a simple qualitative model for conductance. In this context, $f = \langle T_e M_e\rangle/\langle T_c M_c\rangle$, where T_e and T_c are the tunneling probabilities for edge and top contacts, respectively, within the Wentzel–Kramers–Brillouin approximation. T_e and T_c reduce exponentially as the metal–carbon spacing (d_{m-c}) increases. M_e and M_c are the numbers of conducting modes for edge and top contacts, respectively. The number of modes depends on the type of metal and the nature of the contact. For physisorption contact [42], the band structure of graphene is unaffected by the metal, and the number of modes can be calculated by $M(E_F) = 2W|E_F|/\pi\hbar v_f$. W is the width of graphene, E_F is the Fermi level, $\hbar$ is the Planck constant, and v_f is the Fermi velocity. However, for chemisorption interfaces, the metal alters the band structure of graphene, and the number of modes can only be calculated using first-principle calculations. The situation is more complex in metal–MLG structures, as f becomes dependent on the charge distribution in graphene layers and on the interface quality of the contact due to absorbed molecules.

Furthermore, in typical measurement setups such as TLM, four-probe, and cross-bridge Kelvin, it is not possible to measure the value of f. However, an effective contact resistivity (ρ_c and ρ_e) can be measured. In a graphene layer with width W, length L_C, thickness t_{SLG}, and carbon–carbon distance a_{cc}, the total resistance for top contact is $R_T = \rho_c/WL_C = \rho_{c_\mathrm{pc}}/(\#\ of\ atoms\ on\ surface)$, which leads to $\rho_c = 3\sqrt{3}a_{\mathrm{cc}}\rho_{e_\mathrm{pc}}/4$. For edge contact, the total contact resistance is $R_E = \rho_e/Wt_{\mathrm{SLG}} = \rho_{e_\mathrm{pc}}/(\#\ of\ atoms\ on\ edge)$, where the numbers of atoms on edge are $W/\sqrt{3}a_{\mathrm{cc}}$ for zigzag edge and $2W/3a_{\mathrm{cc}}$ for armchair edge. Therefore

$$f = \frac{4}{3}\frac{\rho_c}{\rho_e}\frac{t_{\mathrm{SLG}}}{a_{\mathrm{cc}}}, \qquad \text{for zigzag}$$

$$f = \frac{2}{\sqrt{3}}\frac{\rho_c}{\rho_e}\frac{t_{\mathrm{SLG}}}{a_{\mathrm{cc}}}, \qquad \text{for armchair.}$$

In this work, an average of these values is used for all the edge resistances. It is instructive to look at the effects of variation of f on the performance of metal–MLG structures, which will be provided in the companion paper [71]. The variation of the value of f is within the values predicted by first-principle calculations.

The voltage across the contact resistance at side 4 is $(V_S - V)$, where V is the voltage applied to the metal. The BCs along the y-axis are

$$\text{at } y = 0:\ I_y(x, 0, z) = 0 \tag{6}$$

$$\text{at } y = \frac{w}{2}:\ I_y\left(x, \frac{w}{2}, z\right) = dxdz\frac{V_S - V}{\rho_e}. \tag{7}$$

The BCs along the z-axis are similar to the BCs along the y-axis, except for the value of the contact resistance $\rho_c/dxdy$

$$\text{at } z = 0:\ I_z(x, y, 0) = 0 \tag{8}$$

$$\text{at } z = t:\ I_z(x, y, t) = dxdy\frac{V_S - V}{\rho_c}. \tag{9}$$

The BCs along the x-axis are written for the sides 1 and 3. At side 3, the MLG is tied to V through the edge-contact resistance $\rho_e/dydz$. At side 1, the current along the x-axis is equal to the current along the x-axis in the channel, and V_S is also equal to the potential in the channel, as reflected in

$$\text{at } x = 0:\ I_x(0, y, z) = I_{x,\mathrm{Ch}}(0, y, z)$$
$$V_S(0, y, z) = V_{\mathrm{Ch}}(0, y, z). \tag{10}$$

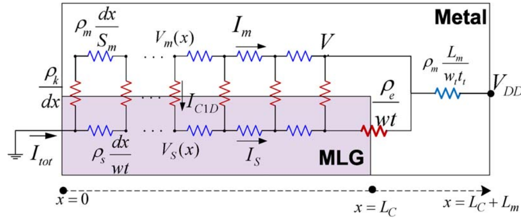

Fig. 4. One-dimensional model for the metal–MLG contact. The resistance ρ_k/dx includes the effects of the sides 2, 4, and 6. The resistance ρ_e/wt is used to model the effect of side 3. The resistances $\rho_s dx/wt$ and $\rho_m dx/S_m$ are used to model the MLG and metal layers, respectively, where S_m is the area of the metal covering MLG, and $\rho_m L_m/w_t t_t$ is used to model the extension of the metal from $x = L_C$ to $x = L_C + L_m$. The geometrical parameters are shown in Fig. 2. I_m and I_S are the currents passing through the metal and MLG, respectively, and I_{C1D} is the current passing through the contact resistance.

The form of the potential in the channel is calculated by solving (5) in the channel using the appropriate BCs in the y- and z-directions. The potential in the middle of the channel was set to $V/2$. Using

$$\text{at } x = L_C: \; I_x(L_C, y, z) = dydz\frac{V_S - V}{\rho_e} \tag{11}$$

the exact value of the potential in the MLG under the contact and in the channel can be calculated.

The solution to (5) using BCs (6)–(11) gives the potential inside the MLG body, which can be used to define the contact resistance

$$V_S(x, y, z) = \sum_{m=1}^{\infty} [(A_m \sinh \beta_m x + B_m \cosh \beta_m x) \cdot \cos \gamma_m y \cdot \cos \lambda_m z] + V \tag{12}$$

$$\beta_m^2 = \gamma_m^2 + \frac{\rho_s}{\rho_I}\lambda_m^2 \tag{13}$$

$$\gamma_m \tan\left(\gamma_m \frac{w}{2}\right) = \frac{\rho_s}{\rho_e} \tag{14}$$

$$\lambda_m \tan(\lambda_m t) = \frac{\rho_I}{\rho_c}. \tag{15}$$

γ_m and λ_m are the solutions to (14) and (15), and β_m is calculated using (13). The parameters A_m and B_m are calculated from (10) and (11). Although the aforementioned solution would be accurate enough with less than 15 modes, the complexity of the solution makes it difficult to interpret the role of different parameters on the potential distribution and the total resistance of the structure. Subsequently, it becomes very difficult to analyze the experimental measurement results with the 3-D model. Therefore, a 1-D model is developed in the following section that includes the effects of all the important factors in the contact resistance.

2) One-Dimensional Model: The 1-D resistive network model is shown in Fig. 4. The contribution of the sides 2, 4, and 6 to the contact resistance is included in the resistive element ρ_k/dx, and the contribution of side 3 to the contact resistance is modeled by the resistive element ρ_e/wt. The MLG sheet is modeled by the horizontal resistors $\rho_s dx/wt$. In this case, the voltage distribution along the y- and z-axes has been neglected, but the effects of nonzero width and thickness will be included in ρ_k later by introduction of width- and thickness-dependent parameters. Only the MLG sheet under the metal electrode is considered. The metal potential at each point is equal to V, because the metal resistivity is zero. First, the equations defining the potential and current in the 1-D model will be described. Then, the 1-D model parameters will be linked to the 3-D model parameters. The current I_S can be calculated by Ohm's law

$$I_S = \frac{-wt}{\rho_s}\frac{dV_S}{dx}. \tag{16}$$

From Kirchhoff's law, at each node in the MLG sheet, $I_S(x + \Delta x) - I_S(x) = (V - V_S)dx/\rho_k$, which can be rearranged as

$$\frac{dI_S}{dx} = \frac{V - V_S}{\rho_k}. \tag{17}$$

Combining (16) and (17), the PDE for the 1-D system can be written as

$$\frac{d^2V_S}{dx^2} - \beta^2 V_S + \beta^2 V = 0 \tag{18}$$

$$\beta^2 = \frac{\rho_s}{wt\rho_k}. \tag{19}$$

The solution to (18) has the general form

$$V_S(x) = A \sinh \beta x + B \cosh \beta x + V. \tag{20}$$

Next, the BCs are defined

$$\text{at } x = 0: \; V_S(0) = 0 \tag{21}$$

$$\text{at } x = L_C: \; I_S(x = L_C) = \frac{V_S(L_C) - V}{\rho_e}wt. \tag{22}$$

By applying the BCs, the constants A and B are calculated

$$B = -V \tag{23}$$

$$A = \frac{\beta\rho_e \tanh \beta L_C + \rho_s}{\rho_s \tanh \beta L_C + \beta\rho_e}V \tag{24}$$

and the total current can be calculated as

$$I_{\text{tot}} = I_S(x = 0) = \frac{-wt\beta}{\rho_s}A. \tag{25}$$

The next step is to link the 1-D model parameters to the 3-D model parameters. The goal is to find ρ_k that leads to the same current distribution in the two models. First, the following resistances are defined:

$$R_T(x) = \frac{\rho_c^*}{wdx} \tag{26}$$

$$R_E(x) = \frac{\rho_e^*}{tdx}. \tag{27}$$

The resistances R_T and R_E are the total resistances to the sides 6 and 2/4, respectively, at any point x along the length on

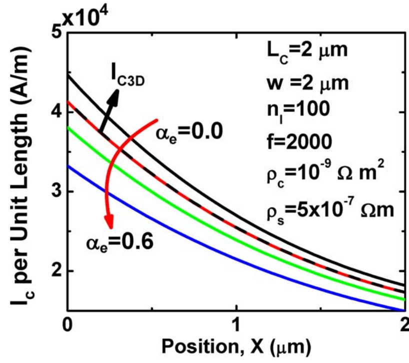

Fig. 5. Demonstration of the effect of variation of α_e on the 1-D approximation of the 3-D system ($\alpha_e = 0.0$, 0.12, 0.3, and 0.6). The current per unit length in the contact is shown along the length. The solid lines show $I_{\rm C1D}$, and the dashed line shows $I_{\rm C3D}$. n_l is the number of graphene layers.

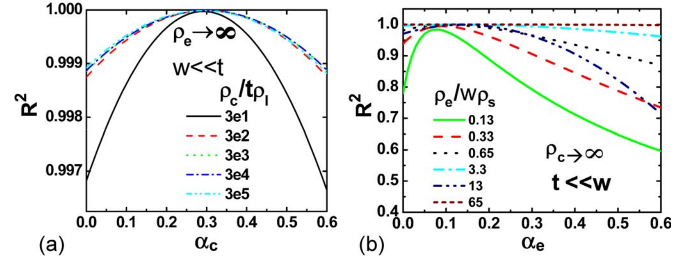

Fig. 6. Comparison of the 1-D model to the 3-D model by observing R^2 through variation of α_c and α_e. A value of R^2 close to one indicates better approximation.

a slab with a length dx. By taking $w \to 0$ and $t \to 0$, the 3-D system converts to a 1-D system, where $\rho_k/dx = R_T \| (R_E/2)$. To account for the nonzero thickness and width of the system, the contact resistivity at edges 2, 4, and 6 is modified in a way similar to that in [69] by a first-order approximation

$$\rho_c^* = \rho_c + \alpha_c t \rho_I \tag{28}$$

$$\rho_e^* = \rho_e + \alpha_e w \rho_s. \tag{29}$$

The addition of the second terms on the right-hand side of (28) and (29) (which depend on the width, thickness, and resistivity of MLG) should approximately account for the voltage drop along the y- and z-axes in MLG. The dimensionless parameters α_c and α_e are used to fit the solutions of the 1-D and 3-D systems. Then, ρ_k is calculated as

$$\rho_k = (R_T \| R_E/2)\, dx = \frac{\rho_c^* \rho_e^*}{2t\rho_c^* + w\rho_e^*}. \tag{30}$$

B. Comparison of the 1-D and 3-D Models and the Validity Range

The coefficients α_c and α_e that were introduced in the previous section are used to model the nonzero width and thickness of the MLG. In this section, the optimum values of these coefficients will be determined by comparing the 1-D and 3-D models, and the validity range of the 1-D model will be investigated. The current distribution per unit length in the contact along the length is used to investigate the accuracy of the model. In the 1-D model, this current is called $I_{\rm C1D}(x)$ as shown in Fig. 4, which is the current per unit length passing through the ρ_k/dx elements ($I_{\rm C1D} = (V - V_S)dx/\rho_k$). In the 3-D model, the corresponding current is called $I_{\rm C3D}(x)$ and is defined as the current per unit length passing from the metal to the MLG at any position x. Hence, $I_{\rm C3D}(x)$ comprises the currents entering MLG from sides 2, 4, and 6.

The current distribution in the contact ($I_{\rm C1D}$ and $I_{\rm C3D}$) is used to compare the 1-D and 3-D models. Fig. 5 shows $I_{\rm C3D}$ for a typical contact structure (dashed line), with $I_{\rm C1D}$ for the same device obtained from (28)–(30) for different values of α_e. It can be observed that, for a specific value of α_e, the 1-D model matches well with the 3-D model. To determine the goodness of the fit, the R-squared (R^2) parameter can be used, which is determined by $R^2 = 1 - SS_{\rm err}/SS_{\rm tot}$, where $SS_{\rm err}$ is the residual sum of squares and $SS_{\rm tot}$ is the total sum of squares. Values of R^2 closer to one correspond to a better fit.

The next step is to find the optimum values of α_e and α_c that produce the best fit for different device geometries and resistivity values. To do so, the coefficients α_c and α_e are varied, and their effect on the fitting of $I_{\rm C1D}$ and $I_{\rm C3D}$ is studied. As stated before, α_c is used to model the nonzero thickness in the z-direction, and α_e is used for the y-direction. Ideally, each of these coefficients should be optimized individually and independent of the other. Therefore, the contact geometry is modified to reduce the effects of potential distribution along the width (height) on the potential distribution along the height (width). For example, it can be observed that, by setting $w \ll t$ and $\rho_e \to \infty$, the majority of the current enters from side 6 in the z-direction, and the potential variation along the y-direction can be neglected; hence, the effect of α_c on $I_{\rm C1D}$ can be studied independent of α_e. Similarly, by setting $t \ll w$ and $\rho_c \to \infty$, the majority of the current passes through sides 2, 3, and 4, and the potential variation along the z-direction can be neglected; hence, the effect of α_e can be studied independently.

Fig. 6 shows R^2 for different values of α_c and α_e using the two configurations discussed earlier. In Fig. 6(a), R^2 is shown for different values of α_c and $\rho_c/t\rho_I$. The reason for the selection of $\rho_c/t\rho_I$ will be discussed later. Different values of resistivity, thickness, and contact length are used to generate the curves. A value of $\alpha_c = 0.3$ yields the best fit. It can be observed that R^2 is not a strong function of α_c. The reason is the relatively small thickness of MLG (and subsequently large values of $\rho_c/t\rho_I$), which leads to small variation of the potential along the z-direction. Similarly, Fig. 6(b) shows how α_e can be optimized for the best fit for different values of $\rho_e/w\rho_s$. A mean value of $\alpha_e = 0.12$ gives the best fit for a wide range of $\rho_e/w\rho_s$. As can be observed, R^2 is a strong function of α_e, which is attributed to the larger MLG width compared to its thickness. A wide range of resistivity, width, and contact length is used to generate the curves.

The validity of the 1-D model depends on the variation of the potential in the y–z plane and subsequently on the gradient of the potential along the y- and z-axes. For a high potential gradient, the linear approximation used for ρ_c^* and ρ_e^* in (28) and (29) cannot model the system accurately. Therefore, the gradient of the potential can be used to study the validity of the 1-D model. On side 2 of MLG (with contact resistivity ρ_e),

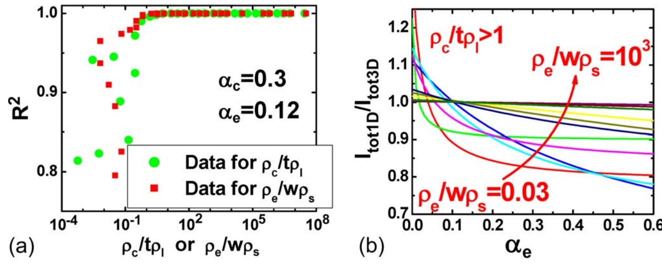

Fig. 7. Range of validity of the 1-D model. (a) Variation of R^2 with $\rho_e/w\rho_s$ and $\rho_c/t\rho_I$ with optimized α_c and α_e values. (b) Comparison of the calculated total currents between the 1-D and 3-D systems. The optimum value of α_e degrades for $\rho_e/w\rho_s < 1$.

the BC for the 3-D model is defined by (7). Combining (2) and (7) and normalizing using $y^* = wy$ yield the potential gradient

$$\frac{dV_S}{dy^*} = \frac{w\rho_s}{\rho_e}(V - V_S). \tag{31}$$

According to (31), a higher value of $\rho_e/w\rho_s$ leads to a smaller gradient of the potential in the y-direction in MLG near side 2 and, hence, smaller I_y. A similar analysis for side 6 shows that the potential gradient in the z-direction is a strong function of $\rho_c/t\rho_I$. That is the reason for the consideration of these two parameters in the optimization of the 1-D fit (Fig. 6).

The optimum values of α_c and α_e were extracted with special conditions on the geometry and resistivity values, which effectively lead to an approximation of the MLG by a 2-D system. To investigate the validity of the approximation for a general 3-D structure, different dimensions and resistivity values are used in simulations, and the 3-D and 1-D models are compared using the parameter R^2. Fig. 7(a) shows R^2 for different contact configurations with the optimized values of α_c and α_e. A wide range of t, w, ρ_c, ρ_I, ρ_e, ρ_s, and L_C is used in the simulations. It can be observed that the 1-D model exhibits a good fit with $R^2 \sim 1$, when the parameters $\rho_e/w\rho_s$ and $\rho_c/t\rho_I$ are larger than one. The value of $\rho_e/w\rho_s$ $(\rho_c/t\rho_I)$ is kept larger than one, when studying $\rho_c/t\rho_I$ $(\rho_e/w\rho_s)$. For values of $\rho_e/w\rho_s$ or $\rho_c/t\rho_I$ less than one, the 1-D approximation fails to model the system accurately.

Fig. 7(b) shows the effect of variation of $\rho_e/w\rho_s$ on the validity of the 1-D model for different values of α_e. $I_{\text{tot1D}} = I_S(0)$ represents the total current in the 1-D model, and I_{tot3D} is the total current passing through the contact in the 3-D model. For a good fit, these two currents should be equal. It can be observed from Fig. 7(b) that the optimum value of α_e degrades from the previously derived value (0.12) for smaller values of $\rho_e/w\rho_s$. These results show that the value of α_e (and similarly α_c) can be modified for a good fit for situations where $\rho_e/w\rho_s$ (or $\rho_c/t\rho_I$) is smaller than one. It should also be noted that the 1-D model works best for $w < 2L_C$, because larger values of w lead to higher variation of the potential along the y-axis compared to the x-axis.

IV. Conclusion

A 1-D model was developed for the metal–MLG contact structure with edge and top contacts. The 1-D model provides simpler insights into the effects of edge and top contacts. The 1-D model was developed along the length of the contact; however, the potential variation along the width and thickness of the structure was also included through a modification of the contact resistivity. Subsequently, the 1-D model was compared to the 3-D system, and the validity range of the 1-D model was discussed. The 1-D model is valid under the following assumptions: 1) ohmic contact between metal and MLG; 2) MLG width larger than 200 nm; 3) contact width less than twice the contact length; 4) low voltage bias (0.1 V); 5) values of $\rho_e/w\rho_s$ and $\rho_c/t\rho_I$ larger than one; and 6) negligible metal resistivity.

The developed model can be used in the design of efficient contacts to MLG and in the characterization of the metal–MLG contact structures where edge and top contacts are present. Using the developed model, it is shown in the companion paper [71] that the edge contacts can significantly reduce the contact resistance of the metal–MLG structures.

References

[1] J.-H. Chen, C. Jang, S. Xiao, M. Ishigami, and M. S. Fuhrer, "Intrinsic and extrinsic performance limits of graphene devices on SiO_2," *Nature Nanotechnol.*, vol. 3, no. 4, pp. 206–209, Apr. 2008.

[2] S. V. Morozov, K. S. Novoselov, M. I. Katsnelson, F. Schedin, D. C. Elias, J. A. Jaszczak, and A. K. Geim, "Giant intrinsic carrier mobilities in graphene and its bilayer," *Phys. Rev. Lett.*, vol. 100, no. 1, pp. 016602-1–016602-4, Jan. 2008.

[3] X. Du, I. Skachko, A. Barker, and E. Y. Andrei, "Approaching ballistic transport in suspended graphene," *Nature Nanotechnol.*, vol. 3, no. 8, pp. 491–495, Aug. 2008.

[4] K. I. Bolotin, K. J. Sikes, Z. Jiang, M. Klima, G. Fudenberg, J. Hone, P. Kim, and H. L. Stormer, "Ultrahigh electron mobility in suspended graphene," *Solid State Commun.*, vol. 146, pp. 351–355, 2008.

[5] T. J. Booth, P. Blake, R. R. Nair, D. Jiang, E. W. Hill, U. Bangert, A. Bleloch, M. Gass, K. S. Novoselov, M. I. Katsnelson, and A. K. Geim, "Macroscopic graphene membranes and their extraordinary stiffness," *Nano Lett.*, vol. 8, no. 8, pp. 2442–2446, 2008.

[6] A. K. Geim and K. S. Novoselov, "The rise of graphene," *Nature Mater.*, vol. 6, pp. 183–191, Mar. 2007.

[7] C. Lee, X. Wei, J. W. Kysar, and J. Hone, "Measurement of the elastic properties and intrinsic strength of monolayer graphene," *Science*, vol. 321, no. 5887, pp. 385–388, Jul. 2008.

[8] International Technology Roadmap for Semiconductors (ITRS). [Online]. Available: http://www.itrs.net

[9] Y. Awano, "Graphene for VLSI: FET and interconnect applications," in *Proc. IEDM*, 2009, pp. 1–4.

[10] C. Xu, H. Li, and K. Banerjee, "Modeling, analysis, and design of graphene nano-ribbon interconnects," *IEEE Trans. Electron Devices*, vol. 56, no. 8, pp. 1567–1578, Aug. 2009.

[11] R. Murali, K. Brenner, Y. Yang, T. Beck, and J. D. Meindl, "Resistivity of graphene nanoribbon interconnects," *IEEE Electron Device Lett.*, vol. 30, no. 6, pp. 611–613, Jun. 2009.

[12] A. Naeemi and J. D. Meindl, "Compact physics-based circuit models for graphene nanoribbon interconnects," *IEEE Trans. Electron Devices*, vol. 56, no. 9, pp. 1822–1833, Sep. 2009.

[13] X. Chen, D. Akinwande, K.-J. Lee, G. F. Close, S. Yasuda, B. C. Paul, S. Fujita, J. Kong, and H. P. Wong, "Fully integrated graphene and carbon nanotube interconnects for gigahertz high-speed CMOS electronics," *IEEE Trans. Electron Devices*, vol. 57, no. 11, pp. 3137–3143, Nov. 2010.

[14] Y. Sui and J. Appenzeller, "Screening and interlayer coupling in multilayer graphene field-effect transistors," *Nano Lett.*, vol. 9, no. 8, pp. 2973–2977, Aug. 2009.

[15] S. Latil and L. Henrard, "Charge carriers in few-layer graphene films," *Phys. Rev. Lett.*, vol. 97, no. 3, pp. 036803-1–036803-4, Jul. 2006.

[16] F. P. Rouxinol, R. V. Gelamo, R. G. Amici, A. R. Vaz, and S. A. Moshkalev, "Low contact resistivity and strain in suspended multilayer graphene," *Appl. Phys. Lett.*, vol. 97, no. 25, pp. 253104-1–253104-3, Dec. 2010.

[17] W. J. Liu, M. F. Li, S. H. Xu, Q. Zhang, Y. H. Zhu, K. L. Pey, H. L. Hu, Z. X. Shen, X. Zou, J. L. Wang, J. Wei, H. L. Zhu, and H. Y. Yu, "Understanding the contact characteristics in single or multi-layer graphene

devices: The impact of defects (carbon vacancies) and the asymmetric transportation behavior," in *Proc. IEDM*, 2010, pp. 560–563.
[18] J. Yu, G. Liu, A. V. Sumant, V. Goyal, and A. A. Balandin, "Graphene-on-diamond devices with increased current-carrying capacity: Carbon sp2-on-sp3 technology," *Nano Lett.*, vol. 12, no. 3, pp. 1603–1608, Mar. 2012.
[19] A. A. Balandin, S. Ghosh, W. Bao, I. Calizo, D. Teweldebrhan, F. Miao, and C. N. Lau, "Superior thermal conductivity of single-layer graphene," *Nano Lett.*, vol. 8, no. 3, pp. 902–907, Mar. 2008.
[20] S. Ghosh, W. Bao, D. L. Nika, S. Subrina, E. P. Pokatilov, C. N. Lau, and A. A. Balandin, "Dimensional crossover of thermal transport in few-layer graphene," *Nature Mater.*, vol. 9, no. 7, pp. 555–558, Jul. 2010.
[21] A. N. Pal and A. Ghosh, "Ultralow noise field-effect transistor from multilayer graphene," *Appl. Phys. Lett.*, vol. 95, no. 8, pp. 082105-1–082105-3, Aug. 2009.
[22] X. Hong, A. Posadas, K. Zou, C. H. Ahn, and J. Zhu, "High-mobility few-layer graphene field effect transistors fabricated on epitaxial ferroelectric gate oxides," *Phys. Rev. Lett.*, vol. 102, no. 13, pp. 136808-1–136808-4, Apr. 2009.
[23] C.-J. Shih, A. Vijayaraghavan, R. Krishnan, R. Sharma, J.-H. Han, M.-H. Ham, Z. Jin, S. Lin, G. L. C. Paulus, N. F. Reuel, Q. H. Wang, D. Blankschtein, and M. S. Strano, "Bi- and trilayer graphene solutions," *Nature Nanotechnol.*, vol. 6, no. 7, pp. 439–445, Jul. 2011.
[24] K. Tang, R. Qin, J. Zhou, H. Qu, J. Zheng, R. Fei, H. Li, Q. Zheng, Z. Gao, and J. Lu, "Electric-field-induced energy gap in few-layer graphene," *J. Phys. Chem. C*, vol. 115, no. 19, pp. 9458–9464, May 2011.
[25] C. H. Lui, Z. Li, K. F. Mak, E. Cappelluti, and T. F. Heinz, "Observation of an electrically tunable band gap in trilayer graphene," *Nature Phys.*, vol. 7, no. 12, pp. 944–947, Sep. 2011.
[26] W. Bao, L. Jing, J. Velasco, Y. Lee, G. Liu, D. Tran, B. Standley, M. Aykol, S. B. Cronin, D. Smirnov, M. Koshino, E. McCann, M. Bockrath, and C. N. Lau, "Stacking-dependent band gap and quantum transport in trilayer graphene," *Nature Phys.*, vol. 7, no. 12, pp. 948–952, Dec. 2011.
[27] J. Gunho, C. Minhyeok, C. Chu-Young, K. Jin Ho, P. Woojin, L. Sangchul, H. Woong-Ki, K. Tae-Wook, P. Seong-Ju, H. Byung Hee, K. Yung Ho, and L. Takhee, "Large-scale patterned multi-layer graphene films as transparent conducting electrodes for GaN light-emitting diodes," *Nanotechnology*, vol. 21, no. 12, p. 175201, Apr. 2010.
[28] X. Wang, L. Zhi, and K. Mullen, "Transparent, conductive graphene electrodes for dye-sensitized solar cells," *Nano Lett.*, vol. 8, no. 1, pp. 323–327, Jan. 2008.
[29] Y. Wang, X. Chen, Y. Zhong, F. Zhu, and K. P. Loh, "Large area, continuous, few-layered graphene as anodes in organic photovoltaic devices," *Appl. Phys. Lett.*, vol. 95, no. 6, pp. 063302-1–063302-3, Aug. 2009.
[30] P. Blake, P. D. Brimicombe, R. R. Nair, T. J. Booth, D. Jiang, F. Schedin, L. A. Ponomarenko, S. V. Morozov, H. F. Gleeson, E. W. Hill, A. K. Geim, and K. S. Novoselov, "Graphene-based liquid crystal device," *Nano Lett.*, vol. 8, no. 6, pp. 1704–1708, Jun. 2008.
[31] J. Wu, M. Agrawal, H. c. A. Becerril, Z. Bao, Z. Liu, Y. Chen, and P. Peumans, "Organic light-emitting diodes on solution-processed graphene transparent electrodes," *ACS Nano*, vol. 4, no. 1, pp. 43–48, Jan. 2009.
[32] Y. Ji, S. Lee, B. Cho, S. Song, and T. Lee, "Flexible organic memory devices with multilayer graphene electrodes," *ACS Nano*, vol. 5, no. 7, pp. 5995–6000, Jul. 2011.
[33] M. Choe, B. H. Lee, G. Jo, J. Park, W. Park, S. Lee, W.-K. Hong, M.-J. Seong, Y. H. Kahng, K. Lee, and T. Lee, "Efficient bulk-heterojunction photovoltaic cells with transparent multi-layer graphene electrodes," *Organic Electron.*, vol. 11, no. 11, pp. 1864–1869, Nov. 2010.
[34] X. Li, Y. Zhu, W. Cai, M. Borysiak, B. Han, D. Chen, R. D. Piner, L. Colombo, and R. S. Ruoff, "Transfer of large-area graphene films for high-performance transparent conductive electrodes," *Nano Lett.*, vol. 9, no. 12, pp. 4359–4363, Dec. 2009.
[35] S. Bae, H. Kim, Y. Lee, X. Xu, J.-S. Park, Y. Zheng, J. Balakrishnan, T. Lei, H. Ri Kim, Y. I. Song, Y.-J. Kim, K. S. Kim, B. Ozyilmaz, J.-H. Ahn, B. H. Hong, and S. Iijima, "Roll-to-roll production of 30-inch graphene films for transparent electrodes," *Nature Nanotechnol.*, vol. 5, no. 8, pp. 574–578, Aug. 2010.
[36] X. Yang, G. Liu, A. A. Balandin, and K. Mohanram, "Triple-mode single-transistor graphene amplifier and its applications," *Mater. Sci.*, vol. 4, no. 10, pp. 5532–5538, Oct. 2010.
[37] X. Yang and G. Liu, "Graphene ambipolar multiplier phase detector," *IEEE Electron Device Lett.*, vol. 32, no. 10, pp. 1328–1330, Oct. 2011.
[38] G. Liu, W. Stillman, S. Rumyantsev, Q. Shao, M. Shur, and A. A. Balandin, "Low-frequency electronic noise in the double-gate single-layer graphene transistors," *Appl. Phys. Lett.*, vol. 95, no. 3, pp. 033103-1–033103-3, Jul. 2009.
[39] G. Liu, S. Rumyantsev, M. Shur, and A. A. Balandin, "Graphene thickness-graded transistors with reduced electronic noise," *Appl. Phys. Lett.*, vol. 100, no. 3, pp. 033103-1–033103-3, Jan. 2012.
[40] R. Golizadeh-Mojarad and S. Datta, "Effect of contact induced states on minimum conductivity in graphene," *Phys. Rev. B*, vol. 79, no. 8, pp. 085410-1–085410-5, Feb. 2007.
[41] P. Zhao, Q. Zhang, D. Jena, and S. O. Koswatta, "Influence of metal–graphene contact on the operation and scalability of graphene field-effect-transistors," *IEEE Trans. Electron Devices*, vol. 58, no. 9, pp. 3170–3178, Sep. 2011.
[42] P. A. Khomyakov, G. Giovannetti, P. C. Rusu, G. Brocks, J. van den Brink, and P. J. Kelly, "First-principles study of the interaction and charge transfer between graphene and metals," *Phys. Rev. B*, vol. 79, no. 19, pp. 195425-1–195425-12, 2009.
[43] C. Gong, G. Lee, B. Shan, E. M. Vogel, R. M. Wallace, and K. Cho, "First-principles study of metal–graphene interfaces," *J. Appl. Phys.*, vol. 108, no. 12, pp. 123711-1–123711-8, Dec. 2010.
[44] Q. Ran, M. Gao, X. Guan, Y. Wang, and Z. Yu, "First-principles investigation on bonding formation and electronic structure of metal–graphene contacts," *Appl. Phys. Lett.*, vol. 94, no. 10, pp. 103511-1–103511-3, Mar. 2009.
[45] J. H. LeeEduardo, K. Balasubramanian, R. T. Weitz, M. Burghard, and K. Kern, "Contact and edge effects in graphene devices," *Nature Nano*, vol. 3, no. 8, pp. 486–490, Aug. 2008.
[46] K. Nagashio, T. Nishimura, K. Kita, and A. Toriumi, "Contact resistivity and current flow path at metal/graphene contact," *Appl. Phys. Lett.*, vol. 97, no. 14, pp. 143514-1–143514-3, Oct. 2010.
[47] J. A. Robinson, M. LaBella, M. Zhu, M. Hollander, R. Kasarda, Z. Hughes, K. Trumbull, R. Cavalero, and D. Snyder, "Contacting graphene," *Appl. Phys. Lett.*, vol. 98, no. 5, pp. 053103-1–053103-3, Jan. 2011.
[48] F. Xia, V. Perebeinos, Y.-M. Lin, Y. Wu, and P. Avouris, "The origins and limits of metal–graphene junction resistance," *Nature Nanotechnol.*, vol. 6, no. 3, pp. 179–184, Feb. 2011.
[49] K. L. Grosse, M.-H. Bae, F. Lian, E. Pop, and W. P. King, "Nanoscale Joule heating, Peltier cooling and current crowding at graphene–metal contacts," *Nature Nanotechnol.*, vol. 6, no. 5, pp. 287–290, May 2011.
[50] B. C. Huang, M. Zhang, Y. Wang, and J. Woo, "Contact resistance in top-gated graphene field-effect transistors," *Appl. Phys. Lett.*, vol. 99, no. 3, pp. 032107-1–032107-3, Jul. 2011.
[51] V. K. Nagareddy, I. P. Nikitina, D. K. Gaskill, J. L. Tedesco, C. R. Eddy, J. P. Goss, N. G. Wright, and A. B. Horsfall, "High temperature measurements of metal contacts on epitaxial graphene," *Appl. Phys. Lett.*, vol. 99, no. 7, pp. 073506-1–073506-3, Aug. 2011.
[52] M. Nagase, H. Hibino, H. Kageshima, and H. Yamaguchi, "Contact conductance measurement of locally suspended graphene on SiC," *Appl. Phys. Exp.*, vol. 3, no. 4, pp. 045101-1–045101-3, Apr. 2010.
[53] R. Nouchi, T. Saito, and K. Tanigaki, "Determination of carrier type doped from metal contacts to graphene by channel-length-dependent shift of charge neutrality points," *Appl. Phys. Exp.*, vol. 4, no. 3, pp. 035101-1–035101-3, 2011.
[54] N. Park, B.-K. Kim, J.-O. Lee, and J.-J. Kim, "Influence of metal work function on the position of the Dirac point of graphene field-effect transistors," *Appl. Phys. Lett.*, vol. 95, no. 24, pp. 243105-1–243105-3, Dec. 2009.
[55] K. N. Parrish and D. Akinwande, "Impact of contact resistance on the transconductance and linearity of graphene transistors," *Appl. Phys. Lett.*, vol. 98, no. 18, pp. 183505-1–183505-3, May 2011.
[56] N. Xu and J. W. Ding, "Conductance growth in metallic bilayer graphene nanoribbons with disorder and contact scattering," *J. Phys., Condens. Matter*, vol. 20, no. 48, p. 485213, Dec. 2008.
[57] Y.-B. Zhou, B.-H. Han, Z.-M. Liao, Q. Zhao, J. Xu, and D.-P. Yu, "Effect of contact barrier on electron transport in graphene," *J. Chem. Phys.*, vol. 132, no. 2, pp. 024706-1–024706-5, Jan. 2010.
[58] S. Barraza-Lopez, M. Vanević, M. Kindermann, and M. Y. Chou, "Effects of metallic contacts on electron transport through graphene," *Phys. Rev. Lett.*, vol. 104, no. 7, pp. 076807-1–076807-4, Feb. 2010.
[59] Y. Matsuda, W.-Q. Deng, and W. A. Goddard, "Contact resistance for "end-contacted" metal–graphene and metal–nanotube interfaces from quantum mechanics," *J. Phys. Chem. C*, vol. 114, pp. 17 845–17 850, 2010.
[60] C. Gong, G. Lee, W. Wang, B. Shan, E. M. Vogel, R. M. Wallace, and K. Cho, "First-principles and quantum transport studies of metal–graphene end contacts," in *Proc. MRS*, 2010, pp. 1259-S14–1259-S35.
[61] G. Liang, N. Neophytou, M. S. Lundstrom, and D. E. Nikonov, "Contact effects in graphene nanoribbon transistors," *Nano Lett.*, vol. 8, no. 7, pp. 1819–1824, Jul. 2008.

[62] D. Berdebes, T. Low, Y. Sui, J. Appenzeller, and M. S. Lundstrom, "Substrate gating of contact resistance in graphene transistors," *IEEE Trans. Electron Devices*, vol. 58, no. 11, pp. 3925–3932, Nov. 2011.

[63] P. Blake, R. Yang, S. V. Morozov, F. Schedin, L. A. Ponomarenko, A. A. Zhukov, I. V. Grigorieva, K. S. Novoselov, and A. K. Geim, "Influence of metal contacts and charge inhomogeneity on transport properties of graphene near the neutrality point," *Solid State Commun.*, vol. 149, no. 27/28, pp. 1068–1071, Jul. 2008.

[64] J. Cayssol, B. Huard, and D. Goldhaber-Gordon, "Contact resistance and shot noise in graphene transistors," *Phys. Rev. B*, vol. 79, no. 7, pp. 0754286-1–0754286-6, Feb. 2008.

[65] A. Hsu, H. Wang, K. K. Kim, J. Kong, and T. Palacios, "Impact of graphene interface quality on contact resistance and RF device performance," *IEEE Electron Device Lett.*, vol. 32, no. 8, pp. 1008–1010, Aug. 2011.

[66] T. Mueller, F. Xia, M. Freitag, J. Tsang, and P. Avouris, "The role of contacts in graphene transistors: A scanning photocurrent study," *Phys. Rev. B*, vol. 79, no. 24, pp. 245430-1–245430-6, Feb. 2009.

[67] A. Venugopal, L. Colombo, and E. M. Vogel, "Contact resistance in few and multilayer graphene devices," *Appl. Phys. Lett.*, vol. 96, no. 1, pp. 013512-1–013512-3, Jan. 2010.

[68] K. Nagashio, T. Nishimura, K. Kita, and A. Toriumi, "Systematic investigation of the intrinsic channel properties and contact resistance of monolayer and multilayer graphene field-effect transistor," *Jpn. J. Appl. Phys.*, vol. 49, no. 5, pp. 051304-1–051304-6, Apr. 2010.

[69] H. Berger, "Models for contacts to planar devices," *Solid State Electron.*, vol. 15, no. 2, pp. 145–158, Feb. 1972.

[70] D. B. Scott, W. R. Hunter, and H. Shichijo, "A transmission line model for silicided diffusions: Impact on the performance of VLSI circuits," *IEEE Trans. Electron Devices*, vol. ED-29, no. 4, pp. 651–661, Apr. 1982.

[71] Y. Khatami, H. Li, C. Xu, and K. Banerjee, "Metal-to-multilayer-graphene contact—Part II: Analysis of contact resistance," *IEEE Trans. Electron Devices*, vol. 59, no. 9, pp. 2453–2460, Sep. 2012.

[72] M. P. Anantram, S. Datta, and Y. Xue, "Coupling of carbon nanotubes to metallic contacts," *Phys. Rev. B*, vol. 61, no. 20, pp. 14 219–14 224, May 2000.

[73] Y. Matsuda, W.-Q. Deng, and W. A. Goddard, "Contact resistance properties between nanotubes and various metals from quantum mechanics," *J. Phys. Chem. C*, vol. 111, no. 29, pp. 11 113–11 116, 2007.

[74] P. Pomorski, C. Roland, and H. Guo, "Quantum transport through short semiconducting nanotubes: A complex band structure analysis," *Phys. Rev. B*, vol. 70, no. 11, pp. 115408-1–115408-5, Sep. 2004.

[75] P. Tarakeshwar and D. M. Kim, "Modulation of the electronic structure of semiconducting nanotubes resulting from different metal contacts," *J. Phys. Chem. B*, vol. 109, no. 16, pp. 7601–7604, Apr. 2005.

[76] A. J. Leggett, "Macroscopic quantum systems and the quantum theory of measurement," *Progr. Theor. Phys. Suppl.*, vol. 69, pp. 80–100, 1980.

[77] K. Matsubara, K. Sugihara, and T. Tsuzuku, "Electrical resistance in the c direction of graphite," *Phys. Rev. B*, vol. 41, no. 2, pp. 969–974, Jan. 1990.

[78] D. Z. Tsang and M. S. Dresselhaus, "The c-axis electrical conductivity of kish graphite," *Carbon*, vol. 14, no. 1, pp. 43–46, 1976.

[79] F. Guinea, "Charge distribution and screening in layered graphene systems," *Phys. Rev. B*, vol. 75, no. 23, pp. 235433-1–235433-7, Jun. 2007.

[80] R. A. Serway, *Principles of Physics*, 2nd ed. London, U.K.: Saunders, 1998, p. 602.

[81] P. M. Solomon, "Contact resistance to a one-dimensional quasi-ballistic nanotube/wire," *IEEE Electron Device Lett.*, vol. 32, no. 3, pp. 246–248, Mar. 2011.

[82] A. D. Franklin, S.-J. Han, A. A. Bol, and W. Haensch, "Effects of nanoscale contacts to graphene," *IEEE Electron Device Lett.*, vol. 32, no. 8, pp. 1035–1037, Aug. 2011.

[83] M. A. Kuroda, J. Tersoff, and G. J. Martyna, "Nonlinear screening in multilayer graphene systems," *Phys. Rev. Lett.*, vol. 106, no. 11, pp. 116804-1–116804-4, Mar. 2011.

[84] A. Sagar, E. J. H. Lee, K. Balasubramanian, M. Burghard, and K. Kern, "Effect of stacking order on the electric-field induced carrier modulation in graphene bilayers," *Nano Lett.*, vol. 9, no. 9, pp. 3124–3128, Sep. 2009.

Yasin Khatami (S'05) received the B.Sc. and M.Sc. degrees in EE from Sharif University of Technology, Tehran, Iran. He is currently working toward the Ph.D. degree at the University of California, Santa Barbara, in the field of graphene electronics and energy-efficient devices.

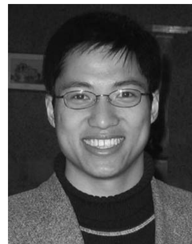

Hong Li (S'07) received the M.S. degree from Shanghai Jiao Tong University, Shanghai, China. He is currently working toward the Ph.D. degree in the Department of Electrical and Computer Engineering, University of California, Santa Barbara.

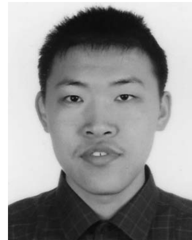

Chuan Xu (S'08–M'12) received the B.S. and the M.S. degrees in microelectronics from Peking University in 2004 and 2007, respectively, and the Ph.D. degree in electrical engineering from University of California, Santa Barbara.

Dr. Xu is now with Maxim Integrated Products, Beaverton, Oregon.

Kaustav Banerjee (S'92–M'99–SM'03–F'12) received the Ph.D. degree in electrical engineering and computer sciences from the University of California, Berkeley, in 1999.

He is currently a Professor in the Department of Electrical and Computer Engineering at the University of California, Santa Barbara, working on nanoelectronics.